Chemical Science

ROYAL SOCIETY OF CHEMISTRY

EDGE ARTICLE

View Article Online
View Journal

Cite this: DOI: 10.1039/d5sc10014c

All publication charges for this article have been paid for by the Royal Society of Chemistry

Engineering the electronic structure of Ni–Co bimetallic sites toward efficient electrochemical biomass upgrading and CO_2 reduction

Qing-Lian Yan,[a] Xun-Bin Lin,[a] Ji-dan Liu,[a] Ting Ouyang*[a] and Zhao-Qing Liu*[ab]

Electrochemical coupling of the 5-hydroxymethylfurfural oxidation reaction (HMFOR) and CO_2 reduction reaction (CO_2RR) offers a promising route to produce high-value chemicals while lowering the energy input. A critical bottleneck in the CO_2-HMF coupled system is the poor ability of the anode catalyst to adsorb and desorb HMF and OH^-, resulting in prohibitively high energy consumption. We construct an anode catalyst $NiCo_2O_4$ by regulating the tetrahedral site to increase the ratio of Co^{3+}/Co^{2+}, which achieves a faradaic efficiency (FE) for 2,5-furandicarboxylic acid (FDCA) of 99.1% at 1.5 V *vs.* RHE. The CO_2-HMF coupled system with $NiCo_2O_4$ as an anode and Au as a cathode at a low cell voltage of 1.7 V affords a total energy conversion efficiency of 43.3%; the FE_{FDCA} of the anode is 91.9%, and the FE of the cathode is 94.7% (66.1% for CO and 28.6% for H_2). *In-situ* surface-enhanced Raman spectroscopy further elucidates the dynamic evolution of the surface state and intermediates of the integrated system: the $NiCo_2O_4$ anode promotes HMF-to-FDCA conversion *via* potential-dependent formation of Ni^{3+} and Co^{3+} intermediates for OH^- capture. Meanwhile, the key intermediate *CO for CO_2-to-CO conversion is detected at the cathode, and the simultaneous progress of the anodic and cathodic reactions significantly reduces the energy consumption of the coupled system. This work provides important theoretical support and a technical approach for the design and amplification of CO_2-HMF coupled systems.

Received 21st December 2025
Accepted 15th January 2026

DOI: 10.1039/d5sc10014c

rsc.li/chemical-science

Introduction

Electrochemical conversion technology provides a green solution for key issues in the field of energy and environment. Among them, water electrolysis hydrogen production (HER system) occupies a core position in the large-scale preparation of hydrogen energy due to the cheap and easy availability of raw materials.[1] Nevertheless, relying on a single method for hydrogen production is insufficient to address the complex challenges of carbon emission reduction and the high-value integration of resources. Using the electrocatalytic CO_2 reduction reaction (CO_2RR) to obtain value-added chemicals represents a critical pathway toward global carbon neutrality.[2–7] However, the practical development of CO_2RR electrolyzers is hindered by the high overpotential of the anodic oxygen evolution reaction (OER), which increases energy consumption and generates low-value byproduct O_2.[8–10] A promising strategy to overcome these limitations involves replacing the OER with the electrooxidation of biomass-derived small molecules. These oxidation reactions not only operate at lower overpotentials but also yield high-value products such as organic acids or fuels.[11–13] By integrating biomass oxidation with the CO_2RR in a single electrolyzer, it could achieve dual benefits: enhanced energy efficiency and simultaneous production of valuable chemicals at both electrodes, thereby advancing sustainable electrochemical synthesis.[14–16]

An electrolyzer system with the anode producing liquid products and the cathode generating gas products is convenient for product detection, separation and collection.[17] A promising candidate for the anodic reaction is 5-hydroxymethylfurfural, an important and impressive biomass derivative.[18] Compared to the OER ($4OH^- + O_2 \rightarrow 2H_2O + 4e^-$, 1.23 V), the HMFOR (HMF + $6OH^- \rightarrow$ FDCA + $4H_2O + 6e^-$, 0.3 V) shows a much lower theoretical potential and produces high-value chemicals.[19–21] HMF can be selectively oxidized or reduced to produce polymer monomers, chemicals and liquid fuels because its structure contains active hydroxyl groups and aldehyde groups. Notably, FDCA is one of the 12 sugar-based platform compounds listed by the U.S. Department of Energy and is obtained through the oxidation of HMF's two oxygen-containing groups into carboxyl groups (Table S1).[18,22–24] Accordingly, coupling the cathodic CO_2RR with the anodic HMFOR is expected to simultaneously produce high value-added chemicals in an electrolytic cell. The half-cell and overall responses involved are shown below.

[a]*School of Chemistry and Chemical Engineering, Institute of Clean Energy and Materials, Key Laboratory for Clean Energy and Materials, Huangpu Hydrogen Innovation Center, Guangzhou University, Guangzhou 510006, P. R. China. E-mail: ouyt@gzhu.edu.cn; lzqgzu@gzhu.edu.cn*

[b]*School of Chemistry, South China Normal University, Guangzhou 510006, P. R. China*

Anodic reaction: $C_6H_6O_3 + 2H_2O \rightarrow C_6H_4O_5 + 6H^+ + 6e^-$

Cathodic reaction: $3CO_2 + 3H_2O + 6e^- \rightarrow 3CO + 6OH^-$

The total reaction: $C_6H_6O_3 + 3CO_2 \rightarrow C_6H_4O_5 + 3CO + H_2O$

Notably, the development of the CO_2-HMF coupled system has attracted considerable attention.[25–27] However, the integrated system of the HMFOR and CO_2RR remains underexplored, with unresolved scientific challenges in understanding the reaction kinetics at both electrodes. Research on this system still faces a key challenge: the current research on the CO_2-HMF coupled system mostly focuses on the independent development and performance optimization of anode and cathode catalysts. However, there is a lack of direct and *in situ* experimental evidence for the dynamic evolution of active sites at both ends of the catalyst, the formation and consumption of key reaction intermediates, and the dynamic synergy mechanism between them under actual working conditions. Co_3O_4 as a HMFOR catalyst has garnered significant attention for its abundant octahedral Co (Co^{3+} O_h) active sites.[28,29] Co^{3+} O_h sites with their high oxidation state, optimized electronic structure, and stable lattice environment, serve as critical active centers for enhancing HMFOR activity and selectivity.[30–32] However, three key limitations hinder their practical application: (1) in the octahedral crystal field, the fully occupied t_{2g}^6 of low-spin Co^{3+} O_h sites results in excessively strong adsorption of HMF molecules, while the activation capability for OH^- remains insufficient. This imbalance impedes the efficient deprotonation of intermediates (such as 5-hydroxymethyl-2-furancarboxylic acid (HMFCA) and 5-formyl-2-furancarboxylic acid (FFCA)); (2) the HMFOR deprotonation process under alkaline conditions relies heavily on the dynamic supply of OH^- on the surface of the catalyst. However, the weak adsorption and activation of OH^- by Co_3O_4 lead to sluggish reaction kinetics; (3) Co^{3+} O_h sites in the spinel structure tend to trigger the OER side reaction and significantly reduce the HMFOR selectivity.

To address the imbalance between HMF adsorption strength and OH^- supply efficiency, doping Co_3O_4 with transition metals (Fe, Zn, Ni…) has become an effective strategy to regulate the electronic and catalytic properties of Co^{3+} O_h sites.[33–35] In this work, a $NiCo_2O_4$ catalyst was synthesized *via* Ni incorporation into Co_3O_4. Systematic electrochemical measurements, *in situ* spectroscopic studies, and theoretical calculations reveal that the Ni sites significantly enhance the concurrent adsorption and activation of HMF and OH^-, thereby accelerating the dehydrogenation and electron-transfer kinetics during the rate-determining FFCA → FDCA step. Consequently, the $NiCo_2O_4$ anode achieves an exceptional FE_{FDCA} of 99.1% at 1.5 V *vs.* RHE, along with a low potential of 1.22 V *vs.* RHE to deliver a current density of 10 mA cm^{-2}. A double-chamber membrane electrolytic cell, based on the CO_2-HMF coupled system, was constructed. It features a gas diffusion electrode and an ion-selective membrane for the efficient separation of FDCA and CO. In the integrated coupled system, when the cell voltage of the $NiCo_2O_4$ catalyst is 1.7 V, the FE_{FDCA} of the anode is 91.9%, the cathode FE is 94.7% (66.1% for CO and 28.6% for H_2), and the total energy conversion efficiency is 43.3%, which proves that the combination of biomass pricing and the CO_2 conversion reaction is very important to reduce the cost of electricity and improve the economic efficiency and the great prospect of producing high value-added chemicals. Furthermore, *in-situ* surface-enhanced Raman spectroscopy (SERS) indicates that the $NiCo_2O_4$ anode promotes HMF-to-FDCA conversion *via* potential-dependent formation of Ni^{3+} and Co^{3+} intermediates for OH^- capture. Meanwhile, the evolution of key intermediates in the CO_2 to *CO pathway is monitored at the cathode and directly reveals the dynamic evolution process of the surface state of the catalyst under operating conditions, confirming the high degree of kinetic synergy between the two ends of the reaction, thereby significantly reducing the overall energy consumption of the system. This work elucidates the synergistic mechanism of the two types of reaction kinetics *in situ* under coupling conditions for the first time, which provides a key experimental basis for optimizing the bifunctional electrocatalytic system and further exploring the coupling reaction mechanism. Through the above research, we aim to provide theoretical support and a technical path for the design and large-scale application of biomass-carbon dioxide co-electrolysis systems and promote the electrosynthesis technology towards the goal of high efficiency.

Results and discussion

Catalyst synthesis and characterization

Based on the above discussion, $NiCo_2O_4$ supported on CC was synthesized by the hydrothermal-calcination method (Fig. S1). NiO and Co_3O_4 were synthesized by the same method as that for the comparison sample. The crystal structure was characterized by X-ray powder diffraction (XRD). The diffraction peaks of NiO, Co_3O_4 and $NiCo_2O_4$ are consistent with the PDF standard cards of NiO (PDF # 44-1159), Co_3O_4 (PDF # 43-1003) and $NiCo_2O_4$ (PDF # 20-0781), respectively (Fig. S2), indicating that the materials were successfully synthesized. The morphology of the obtained electrocatalysts is observed by scanning electron microscopy (SEM) and transmission electron microscopy (TEM). The SEM image of NiO shows that its structure is a linear cluster, and Co_3O_4 shows a nanosheet array structure (Fig. S3b and c). $NiCo_2O_4$ exhibits a nanoneedle array structure (Fig. S3a). HRTEM images enlarge the blue framed area of a single nanosheet and show clear lattice fringes with a spacing of 0.234 nm, which corresponds to the (111) crystal plane of $NiCo_2O_4$ (Fig. S4). The selected area electron diffraction (SAED) patterns correspond to (111), (220), (311), (222) and (400) crystal planes (Fig. S5), which is consistent with the results of XRD and HRTEM. The corresponding element mapping image displays that the Ni, Co and O elements on the surface of the catalyst are evenly distributed (Fig. S6). The above analysis indicates the successful synthesis of $NiCo_2O_4$. Furthermore, it can be seen from TEM that the (222) crystal plane is the main unit cell of $NiCo_2O_4$. The analysis of the unit cell configuration of the (111) crystal plane of Co_3O_4 and $NiCo_2O_4$ in Fig. 1a preliminarily speculates that the octahedral interstitial Co^{3+} with strong

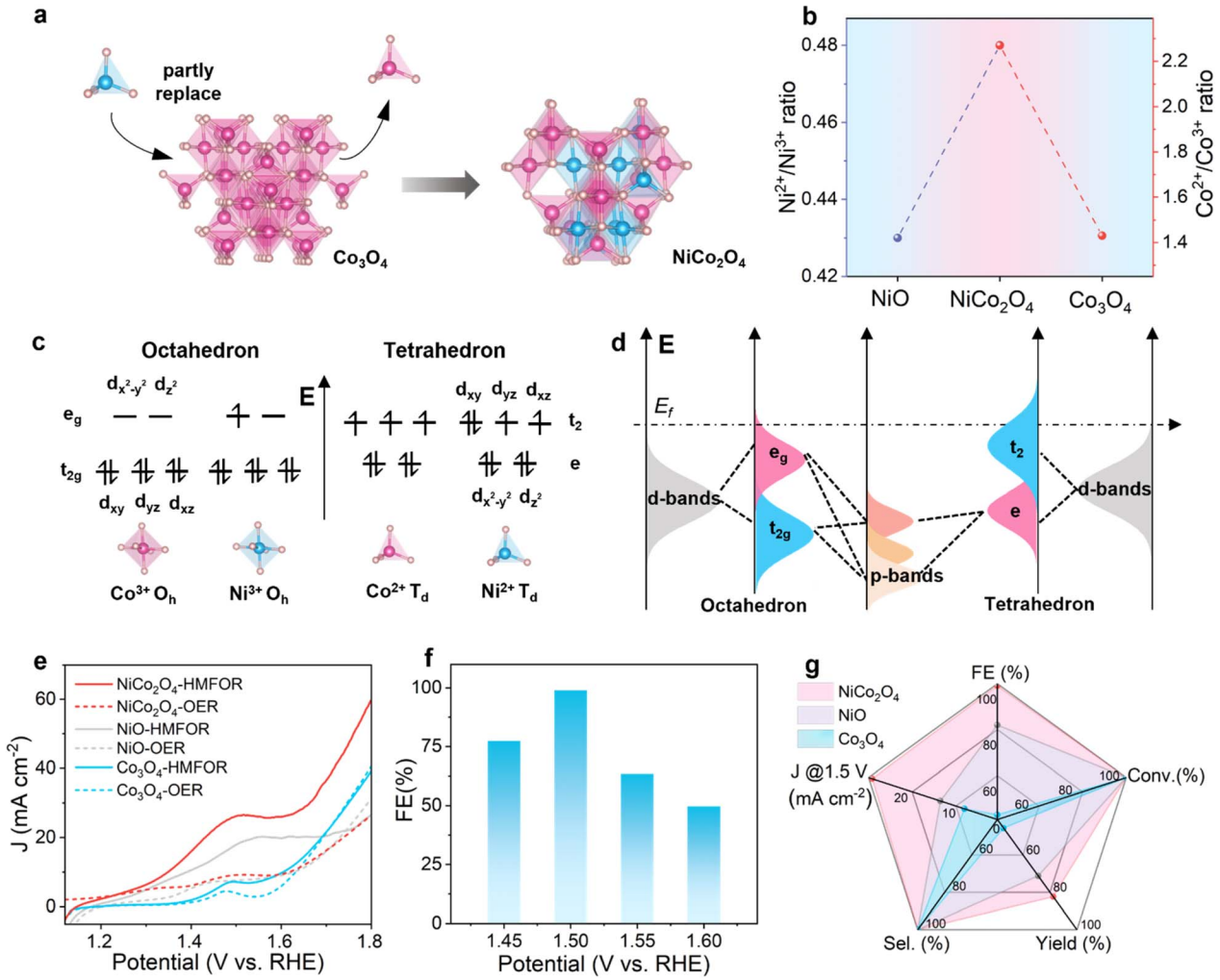

Fig. 1 (a) Lattice structures of Co_3O_4 and $NiCo_2O_4$. (b) The Ni^{2+}/Ni^{3+} ratio and the Co^{2+}/Co^{3+} ratio obtained from XPS for corresponding samples. (c) Schematic electron distribution of the tetrahedron coordination compared to octahedron coordination. (d) Interaction mode of Ni, Co-d and adsorbed molecule p-orbitals in octahedral and tetrahedral configurations. (e) LSV curves with and without 10 mM HMF. (f) FE_{FDCA} of the $NiCo_2O_4$ at different potentials. (g) HMFOR performance comparison of NiO, Co_3O_4 and $NiCo_2O_4$.

adsorption to HMF, after the Ni^{2+} preferentially replaces the tetrahedral interstitial Co^{2+}. After that, the unit cell locally forms an 'octahedral interstitial Co^{3+}-tetrahedral interstitial Ni^{2+}' adjacent coordination structure. Because the oxidation of Co^{3+} is much stronger than that of Ni^{2+}, in order to maintain the charge balance and reduce the lattice energy, Ni^{2+} will transfer the outer electrons to Co^{3+} through the O^{2-} bond, and finally Co^{3+} is reduced to Co^{2+} (still occupying the octahedral gap). Ni^{2+} may be oxidized to Ni^{3+} (maintaining the tetrahedral/octahedral gap), and the electrons realize the directional flow between the adjacent ions in the tetrahedral-octahedral gap. The increase in Co^{3+} electron cloud density further strengthens the adsorption of HMF, and the introduced high-energy d orbital of Ni^{2+} contributes to the desorption of the product. In order to investigate the effect of Ni introduction on the oxidation state of Co, X-ray photoelectron spectroscopy (XPS) measurements were performed on NiO, Co_3O_4, and $NiCo_2O_4$ samples (Fig. S7). The Ni 2p spectra of NiO and $NiCo_2O_4$ (Fig. S8a) show two spin–orbit binaries (Ni $2p_{3/2}$ and Ni $2p_{1/2}$), belonging to Ni^{3+} (855.5 eV and 873.7 eV) and Ni^{2+} (853.7 eV and 871.7 eV) peaks. The Co 2p spectra of Co_3O_4 and $NiCo_2O_4$ (Fig. S8b) show two spin–orbit binary peaks (Co $2p_{3/2}$ and Co $2p_{1/2}$), belonging to Co^{3+} (779.2 eV and 794.3 eV) and Co^{2+} (780.6 eV and 795.9 eV) peaks. As shown in Fig. 1b, the ratio of Ni^{2+}/Ni^{3+} (0.48/1) in $NiCo_2O_4$ is higher than that in NiO (0.43/1). At the same time, the ratio of Co^{2+}/Co^{3+} in $NiCo_2O_4$ (2.27) increases compared with Co_3O_4 (1.43). The above results show that after introducing Ni into Co_3O_4, electrons can be transferred from Ni to Co and promote the reduction of Co^{3+} to Co^{2+}, and Co^{3+} reversely induces the equilibrium results of Ni^{2+} oxidation and Ni-induced Co^{3+} reduction. Next, the spinel cell composition of Co_3O_4 and $NiCo_2O_4$ and the corresponding d-orbital electron filling are understood, which is conducive to the interpretation of the experimental results. The effect of Ni introduction on the molecular configuration of Co_3O_4 was further explored. The d-orbital electron filling orbital distribution maps of the Ni and

Co tetrahedron and octahedron were Co^{3+} O_h (t_{2g}^6), Ni^{3+} O_h (t_{2g}^6 e_g^1), Co^{2+} T_d (e^4 t_2^3), and Ni^{2+} T_d (e^4 t_2^4) (Fig. 1c and d). It is worth noting that the energy level of the splitting d orbital in the octahedral field is t_{2g} (d_{xy}, d_{yz}, d_{xz}) < e_g ($d_{x^2-y^2}$, d_{z^2}), while the energy level of the splitting d-orbital in the tetrahedral field is opposite, e ($d_{x^2-y^2}$, d_{z^2}) < t_2 (d_{xy}, d_{yz}, d_{xz}). Compared with the octahedral coordination, the tetrahedral coordination has three high-energy t_2 (d_{xy}, d_{yz}, d_{xz}) orbitals. More high-energy d-orbitals near the Fermi level provide more opportunities to interact with reactants and intermediates, thus providing a better ability to adjust the catalytic performance.[36,37]

HMFOR performance evaluation

The HMFOR of NiO, Co_3O_4 and $NiCo_2O_4$ was evaluated in a standard three-electrode system. The screening experiments of different concentrations of HMF show that the activity increased with the increase in the HMF concentration (0−40 mM), indicating that the reaction behavior is concentration-dependent (Fig. S9). In order to further study the electro-oxidation behavior and reaction mechanism, 10 mM HMF was selected. Fig. 1e shows the linear sweep voltammetry (LSV) curves of NiO, Co_3O_4 and $NiCo_2O_4$ in the OER and HMFOR. For the OER (dotted line), the curves of Co_3O_4 and $NiCo_2O_4$ both have a peak at 1.49 V *vs.* RHE, which corresponds to the oxidation of Co^{2+} to form high valence Co^{3+} species at potential. The peak at 1.44 V *vs.* RHE in the curve of NiO corresponds to the high valence Ni^{3+} species formed by the oxidation of Ni^{2+} at the potential.[38] When 10 mM HMF is introduced into the electrolyte, the $NiCo_2O_4$ electrode reaches 10 mA cm^{-2} at 1.35 V *vs.* RHE, which is lower than that of NiO (1.39 V) and Co_3O_4 (1.6 V), indicating that the HMFOR performance of $NiCo_2O_4$ is better. When the feed ratio of Ni : Co is 1 : 1, compared with the morphology and LSV response of $NiCo_2O_4$ (Fig. S10 and S11), it further indicates that the introduction of Ni greatly improves the HMFOR performance of Co_3O_4. Under the same conditions, the Tafel slope of $NiCo_2O_4$ (255 mV dec^{-1}) is smaller than that of Co_3O_4 (398 mV dec^{-1}) and NiO (400 mV dec^{-1}, Fig. S12), which also verifies that the HMFOR performance of $NiCo_2O_4$ is better than that of Co_3O_4 and NiO from the kinetic point of view. $NiCo_2O_4$ was evaluated by measuring the electrochemical double layer capacitance (C_{dl}), where a larger C_{dl} means a larger specific surface area and, consequently, more exposed active sites under set conditions. $NiCo_2O_4$ shows a higher C_{dl} value (3.78 mF cm^{-2}) than NiO (2.65 mF cm^{-2}) and Co_3O_4 (1.88 mF cm^{-2}, Fig. S13). The larger ECSA value indicates that $NiCo_2O_4$ has more specific surface area of reaction, which is beneficial for the improvement of HMFOR activity.

The FE_{FDCA} of $NiCo_2O_4$ was tested at 1.45–1.60 V *vs.* RHE (Fig. 1f). With the increase in potential, the FE_{FDCA} decreases gradually due to the emergence of the competitive OER. It is worth noting that the highest FE_{FDCA} is 99.1% at 1.5 V *vs.* RHE. The substances present and composition of the electrolyte at this potential were determined by HPLC-MS. The results show that there is only one substance present (FDCA), indicating that HMF is completely converted into FDCA, and the electro-oxidation process does not stay in the intermediate product step, further indicating the reliability of the data (Fig. S14). A complete comparison of the current density, HMF conversion, FDCA and FE yields and selectivity at 1.5 V *vs.* RHE is revealed in the radar plot (Fig. 1g), indicating that $NiCo_2O_4$ in NiO, Co_3O_4 and $NiCo_2O_4$ has significant HMFOR activity. The current density on the $NiCo_2O_4$ electrode reaches 26.2 mA cm^{-2} at 1.5 V *vs.* RHE, which is much higher than the same voltage on the Co_3O_4 electrode (7.05 mA cm^{-2}) and the NiO electrode (18 mA cm^{-2}). This result indicates that $NiCo_2O_4$ significantly boosts HMFOR efficiency and facilitates electron transfer. The conversion of HMF on NiO, Co_3O_4 and $NiCo_2O_4$ electrodes is 100%, but it is worth noting that the FE_{FDCA} is 99.1% and the yield is 82.44%, which are higher than those of the NiO electrode (82%/71.24%) and Co_3O_4 electrode (43.09%/45.58%). According to the FE of Co_3O_4 which is less than the yield, it is preliminarily speculated that it is more conducive to the formation of intermediate products, namely hydroxyl oxidation. The FE of NiO is lower than its yield, which is more conducive to the formation of FDCA, namely aldehyde oxidation. From the perspective of product collection, the introduction of Ni changes the configuration of Co_3O_4, which greatly improves the HMFOR efficiency of $NiCo_2O_4$.

Corroboration of the reaction pathway

At present, there are two main oxidation pathways of the HMFOR in alkaline electrolyte: 2,5-diformylfuran (DFF) and HMFCA (Fig. 2a).[16,39] In the DFF-directed pathway, the hydroxyl groups of HMF are preferentially oxidized to form DFF, and DFF is further oxidized to FFCA by aldehyde oxidation. In the HMFCA-oriented pathway, HMF is preferentially oxidized by the aldehyde group to form HMFCA and then oxidized by the hydroxyl group to form FFCA. Finally, FDCA is obtained by deep oxidation of FFCA. The $NiCo_2O_4$-catalyzed HMFOR was used to elucidate the reaction pathways involved at 1.5 V *vs.* RHE, and traces of HMF consumption and product (HMFCA, FFCA, DFF and FDCA) accumulation were tracked by HPLC (Fig. 2b and S15). In 1 M KOH containing 7.7 mM HMF (15 mL), a decrease in HMF and an increase in FDCA are observed with the accumulation of charge, indicating that HMF could be converted into FDCA by $NiCo_2O_4$ (Fig. S16 and S17). The color change of the reaction solution during the specific experiment also confirmed the complete conversion process (Fig. S18). In addition to HMF and FDCA, the intermediate products HMFCA and FFCA can be clearly detected, confirming that the conversion of HMF to FDCA follows the HMFCA-oriented pathway (HMF → HMFCA → FFCA → FDCA). In order to further determine the conversion pathway of the HMFOR catalyzed by $NiCo_2O_4$, potential- and time-dependent *in situ* FTIR spectroscopy was used.[40–42] As shown in Fig. 2c–e, $NiCo_2O_4$ has a band at 1654 cm^{-1} (HMF), indicating that HMF is consumed first and then adsorbed, while the downward band of Co_3O_4 has the largest change, and NiO has no obvious change, indicating that Co_3O_4 has the largest adsorption of HMF and NiO has no adsorption. At the same time, fork-like bands at 1523 and 1541 cm^{-1} are observed, indicating the formation of intermediate HMFCA (Fig. S19). With time, a new peak appeared at 1700 cm^{-1}, which

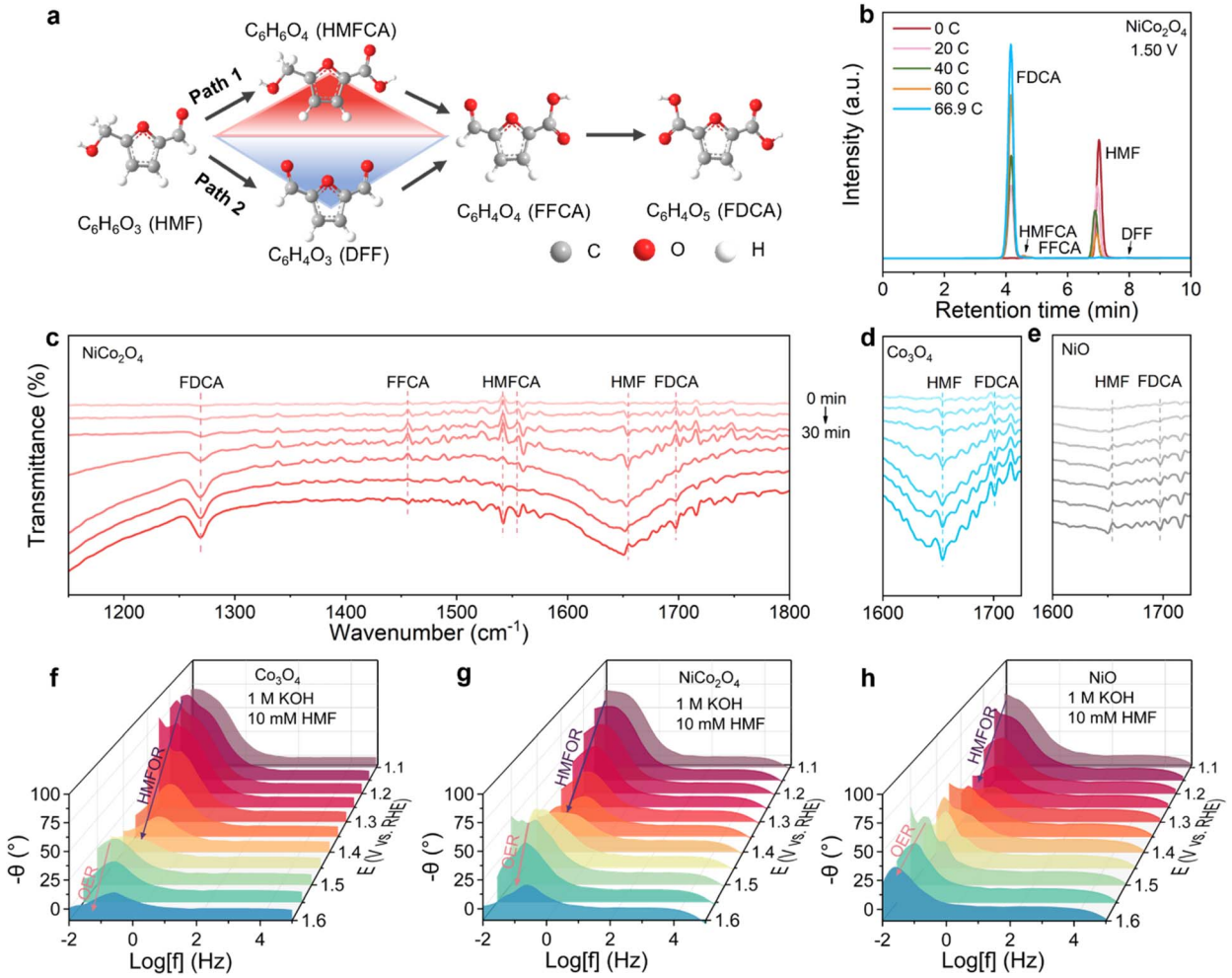

Fig. 2 (a) Two possible reaction pathways for the HMFOR. (b) HPLC chromatogram of oxidation products during the HMFOR at 1.5 V *vs.* RHE. *In situ*-FTIR spectra of $NiCo_2O_4$ (c), Co_3O_4 (d) and NiO (e) samples. Bode plots of Co_3O_4 (f), $NiCo_2O_4$ (g) and NiO (h) samples for the HMFOR.

belongs to the carboxylate group, which is related to the formation of FDCA. $NiCo_2O_4$ has the most obvious change in the descending section, indicating that the formation of FDCA is the fastest. These results indicate that the introduction of Ni with strong desorption of weakly adsorbed reactants on Co_3O_4, which has strongly adsorbed reactants and difficult to desorb products, can result in the HMFOR with efficient multi-electron transfer and dual-site synergistic catalysis of strong adsorption of Co and strong desorption of Ni. In particular, the absence of the DFF signal once again confirms the dominant position of the HMFCA pathway in the $NiCo_2O_4$-catalyzed HMFOR, which is consistent with the results of HPLC analysis. As mentioned, the absence of DFF features is likely to be caused by spontaneous conversion in strongly alkaline solutions.[43,44] In addition, $NiCo_2O_4$ shows excellent catalytic stability and can be recycled four times continuously (Fig. S20a and b), and the conversion rate, yield and FE are all greater than 95%, which can be attributed to its good structural integrity. After the HMFOR test, the stability of the structure and composition was evaluated by a number of characterization studies. The SEM image shows that the overall outline of the needle-like array structure of $NiCo_2O_4$ is well maintained (Fig. S21), and the results show that $NiCo_2O_4$ has a stable microstructure. The XRD pattern shows that $NiCo_2O_4$ retained the original characteristic diffraction peak, and no new peak appeared (Fig. S22), indicating that the crystal structure of the catalyst did not change significantly after the HMFOR. The surface state of the elements was studied by XPS analysis. The subtle changes in the high-resolution XPS spectra of Co and Ni indicate a subtle change in the surface chemical state of $NiCo_2O_4$ (Fig. S23). All these analyses demonstrate the excellent robustness of $NiCo_2O_4$ in the HMFOR.

In-situ electrochemical impedance spectroscopy (EIS) tests were performed on NiO, Co_3O_4 and $NiCo_2O_4$ in 1 M KOH or 1 M KOH + 10 mM HMF under a potential gradient of 1.1–1.6 V *vs.* RHE. The HMFOR and OER processes of NiO, Co_3O_4 and $NiCo_2O_4$ show similar trends in the high-frequency and medium-frequency regions (10–10^5 Hz) (Fig. 2f–h and S24a–c). During the OER process, the Bode plots of NiO, Co_3O_4 and $NiCo_2O_4$ show characteristic peaks in the low-frequency region (0.1–10 Hz). When the potential increases to 1.5 V *vs.* RHE, an inflection point appears in the low frequency region, which may

be related to the adsorption of hydroxyl groups on the surface and surface oxidation, because the initial potential of the OER is in this potential range. The relevant equivalent circuit and Nyquist diagram and the fitted R_{ct} values are shown and summarized (Fig. S25, S26 and Tables S2–S7). By comparison, the introduction of Ni into Co_3O_4 effectively reduces the transfer resistance and results in a faster reaction rate.

In-depth understanding of HMFOR performance

The oxidation of HMF in alkaline solution requires the participation of OH^- species.[45,46] The adsorption and conversion of OH^- is an essential step in the HMFOR, similar to the first step of electrocatalytic water oxidation in an alkaline environment. Therefore, it is necessary to clarify the transformation behavior of OH^- by exploring the OER performance of the material. The Tafel slope of $NiCo_2O_4$ (373 mV dec^{-1}) is larger than that of Co_3O_4 (207 mV dec^{-1}) and NiO (320 mV dec^{-1}) (Fig. S27), indicating that the introduction of Ni inhibits the OER kinetics of $NiCo_2O_4$, that is, inhibits the conversion of OH^- on the surface of $NiCo_2O_4$. The O 1s XPS spectra of different samples can be deconvoluted into three parts (Fig. 3a and b), which are surface adsorbed water molecules (530.2 eV), oxygen vacancies (528.3 eV) and lattice oxygen atoms combined with metal ions (526.8 eV). Compared with the high-resolution spectra of NiO and Co_3O_4, the proportion of lattice oxygen (526.8 eV) in $NiCo_2O_4$ is significantly reduced, and the proportion of absorbed water (530.2 eV) is significantly increased, which confirms the existence of abundant oxygen vacancies in $NiCo_2O_4$. The ratio of lattice oxygen to adsorbed oxygen in $NiCo_2O_4$, Co_3O_4 and NiO samples is 2.6 : 1, 6.7 : 1 and 9.2 : 1, respectively. The results show that the proportion of adsorbed oxygen species in $NiCo_2O_4$ is significantly higher than that in Co_3O_4 and NiO, indicating that $NiCo_2O_4$ may have better adsorption capacity for oxygen-containing species OH^-, which is more conducive to the HMFOR. In the *in-situ* FTIR spectra (Fig. 3c), in the range of 3100−3600 cm^{-1}, NiO shows little change in the intensity of the O–H vibration peak and $NiCo_2O_4$ shows higher O–H vibration peak intensity than Co_3O_4, indicating that more OH^- species are formed or accumulated on the surface of $NiCo_2O_4$ during the reaction, while there is no OH^- accumulation on the surface of NiO. At the same time, it is detected that when the voltage was turned off at the end, the O–H characteristic signals of Co_3O_4, $NiCo_2O_4$ and NiO did not decrease or disappear (Fig. S28). The peak intensity, peak shape and peak position remain stable, which is completely consistent with the characteristics in the process of electrification. This indicates that this process does not involve the physical adsorption of free OH in the electrolyte, but involves the process of chemical combination of active sites on the catalyst surface with OH to form M-OH. The generated M-OH is part of the chemical structure of the catalyst surface and has a stable chemical bonding state. Next, $NiCo_2O_4$ and Co_3O_4 were further explored, and the adsorption activity of OH^- was also determined in an OH^- deficient environment (1 M PBS). The results show that the OER performance of $NiCo_2O_4$ is much higher than that of Co_3O_4 (Fig. 3d), which also proves that the introduction of Ni is particularly beneficial for the capture of OH^-. In Fig. 3e, $NiCo_2O_4$ (−27.5 mV) shows a more negative zeta potential value than Co_3O_4 (−9.5 mV) in the KOH environment, representing more OH^- in the inner Helmholtz layer, which also supports the above conclusion. In addition, in the cyclic voltammetry (CV) curve (Fig. 3f, g and S29), an obvious oxidation peak can be observed in the potential range of 0.8–1.05 V *vs.* RHE, indicating the adsorption of *OH. At the same time, the linear fitting results show that the process is an adsorption control process (Fig. S30 and S31).

Open circuit potential (OCP) was measured to detect changes in the internal organic adsorbent content of the Helmholtz layer. When 10 mM HMF is injected, although the OCP change of $NiCo_2O_4$ (0.536 V) is close to that of Co_3O_4 (0.548 V), the OCP potential of Co_3O_4 of $NiCo_2O_4$ is significantly smaller, indicating that more HMF molecules are inherently adsorbed in the inner Helmholtz layer. As shown in Fig. 3h, the OCP of $NiCo_2O_4$ decreases faster after the addition of HMF, which also means that the introduction of Ni is beneficial for the dynamic adsorption of HMF. The evidence of whether Co^{3+} is the active site of the HMFOR is further investigated. Therefore, we conducted a Co^{3+} elimination time test to explore the function of Co^{3+} species in the HMFOR. As shown in Fig. 3i, $NiCo_2O_4$ is first oxidized to form Co^{3+} species and accumulate at an oxidation potential of 1.1 V *vs.* RHE, resulting in the enrichment of Co^{3+}, which is completed in 1 M KOH + 10 mM HMF. When accumulated to a certain extent, the potential is converted to OCP, and the potential gradually decreases, indicating the attenuation of Co^{3+}. When an additional amount of HMF (50 mM) is introduced into the backward system in the first 10 s, the decay rate of Co^{3+} increases sharply, and the decay time is shortened from about 284 s to 55 s, indicating that Co^{3+} is the active site of the HMFOR.

Density functional theory calculations

In order to further reveal the introduction of Ni, that $NiCo_2O_4$ has a significant improvement in the selectivity and performance of HMF oxidation to FDCA and the internal promotion mechanism for the integration of $NiCo_2O_4$ in the HMFOR, we performed DFT calculations.[47] According to the optimized stable structures of Co_3O_4 and $NiCo_2O_4$, the (111) crystal plane of the catalyst sample is selected for calculation. After adsorption of HMF (Fig. 4a), $NiCo_2O_4$ (0.143 e^-) transferred more electrons to HMF than Co_3O_4 (0.112 e^-), indicating a stronger interaction with HMF. Considering that the appropriate adsorption behavior of OH^- and HMF is critical to the HMFOR performance, the bonding strength of OH* and HMF* at different sites on the sample was evaluated (Fig. 4b, S32 and Tables S8, S9). For the adsorption of OH*, the Co sites of $NiCo_2O_4$ (−1.14 eV) show a smaller bonding strength than the Ni sites of $NiCo_2O_4$ (−0.70 eV) and the Co sites of Co_3O_4 (−1.05 eV). However, for the adsorption of HMF, the Co sites of $NiCo_2O_4$ (−2.55 eV) exhibit more negative adsorption energy than the Ni sites of $NiCo_2O_4$ (−1.84 eV) and the Co sites of Co_3O_4 (−1.96 eV), indicating that the introduction of Ni enhances the adsorption behavior of HMF and OH* on the Co sites of $NiCo_2O_4$, while the Ni sites of $NiCo_2O_4$ exhibit worse

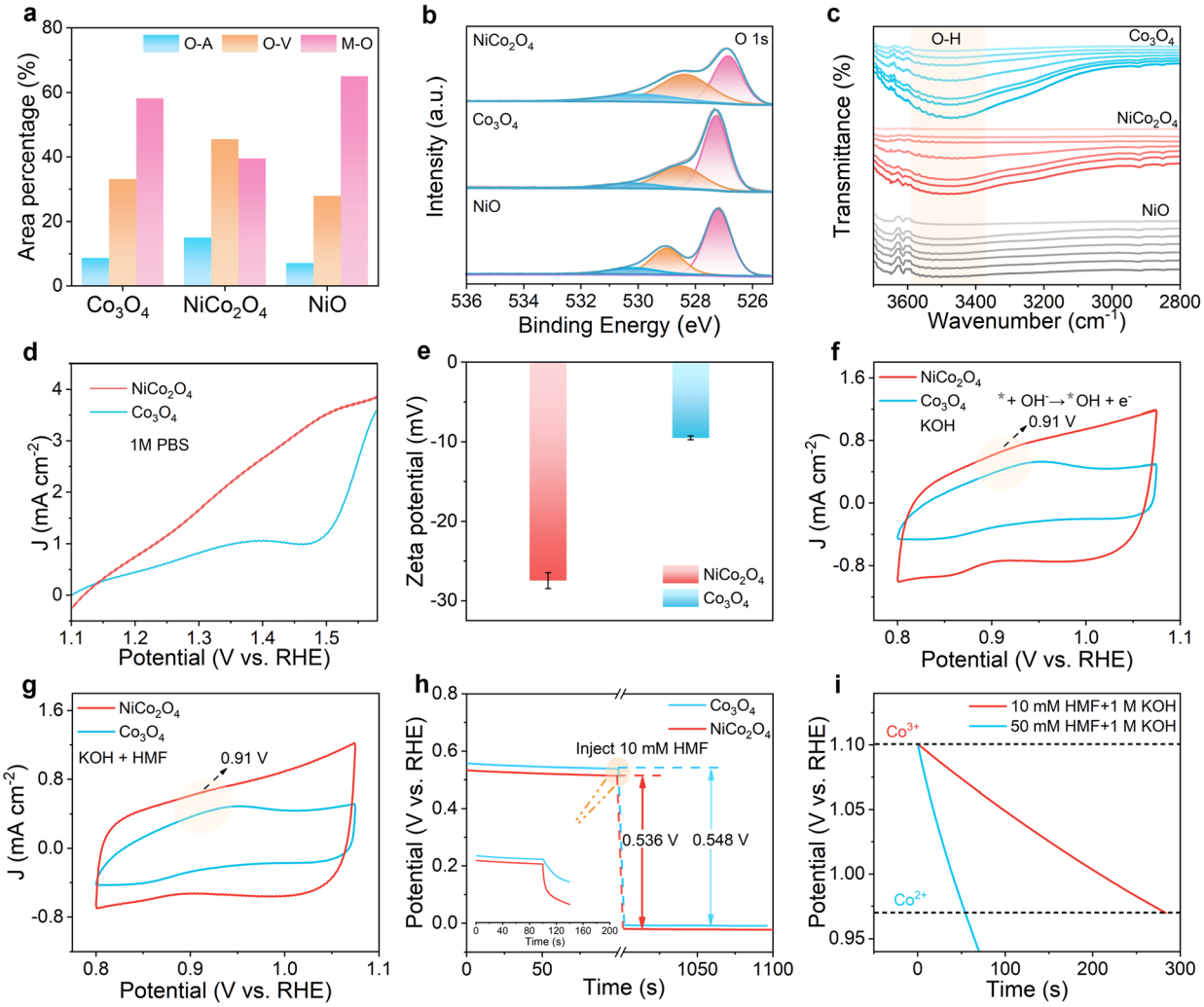

Fig. 3 (a) Relative content of oxygen vacancies, M-O, and adsorbed oxygen groups in the above samples. (b) High-resolution O 1s XPS spectra of NiO, Co_3O_4 and $NiCo_2O_4$. (c) The *in-situ* FTIR spectra of NiO, Co_3O_4 and $NiCo_2O_4$ samples recorded at 1.5 V *vs.* RHE for 30 min in the HMFOR. (d) LSV curves of the Co_3O_4 and $NiCo_2O_4$ samples in 1 M PBS solution. (e) Zeta potential of the Co_3O_4 and $NiCo_2O_4$ samples. CV curves of the Co_3O_4 and $NiCo_2O_4$ samples in (f) KOH and (g) KOH + HMF solution. (h) The OCP of the Co_3O_4 and $NiCo_2O_4$ samples in 1 M KOH solution before and after HMF was injected. (i) Co^{3+} obliteration time test for $NiCo_2O_4$.

HMF and OH* adsorption behavior than the Co sites of Co_3O_4, which just balances the competitive adsorption of HMF molecules and OH^- species, a reaction conducive to subsequent steps. In addition, the total density of states (TDOS) of $NiCo_2O_4$ near the Fermi level (EF) is significantly higher than that of Co_3O_4 due to the introduction of Ni (Fig. 4c and d), indicating that the conductivity of $NiCo_2O_4$ is enhanced, which is conducive to achieving faster interfacial electron transfer in the electrocatalytic process, thus effectively promoting the elementary steps involved in multi-electron transfer in the HMFOR, especially the rate-determining step. The smoother electron supply directly reduces the electron transfer energy barrier, thereby improving the overall reaction kinetics. The partial density of states (PDOS) analysis shows that both Co-3d and Ni-3d orbitals have a major contribution to TDOS, and there are strong peaks and signals near EF, indicating that Ni as an active site promotes electron transfer and has a lower energy barrier. After the introduction of Ni, the d-band center (−2.796 eV) of Co in $NiCo_2O_4$ is slightly shifted upward compared with Co_3O_4 (−2.814 eV), indicating that its interaction with adsorbed oxidation intermediates is strengthened, which is consistent with the strengthening of OH* adsorption behaviour. Then, the reaction state of the HMFOR process on the sample was studied (Fig. 4e–g, S33 and Tables S10–S14), which shows the specific adsorption configuration with the lowest energy path and the corresponding intermediate. Since the HMFOR is an exothermic reaction from HMF → HMF* → HMFCA* → FFCA* FDCA* and HMF → HMF* → DFF* → FFCA* → FDCA*, and the last step FDCA* → FDCA is an endothermic reaction, the HMF adsorption and FDCA desorption steps are determined as the reaction rate-determining steps (RDSs). For HMF adsorption, the Co sites of $NiCo_2O_4$ adsorb HMF to form HMF* with the lowest energy. Combined with the comparison of adsorption configurations, it can be seen that the Co sites of

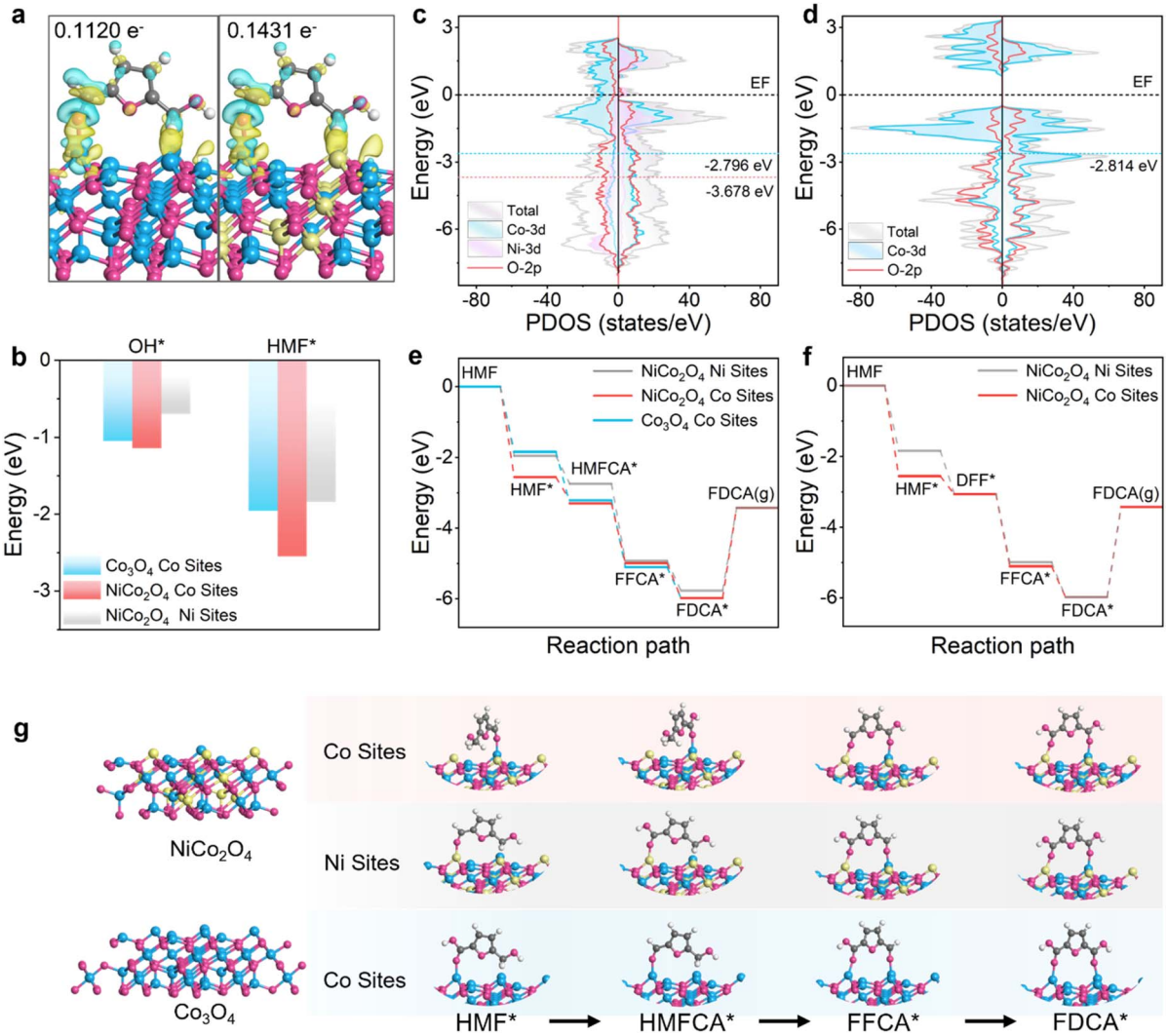

Fig. 4 (a) The calculated charge density difference (CDD) of HMF adsorbed on Co_3O_4 (111) (left) and $NiCo_2O_4$ (111) (right) surfaces, which was calculated using the following equation: $\Delta\rho = \rho(\text{total}) - \rho(\text{surface}) - \rho(\text{HMF})$. The yellow region represents electron accumulation, while the blue region represents electron depletion. (b) The adsorption energies of HMF* and OH* on Ni sites and Co sites of $NiCo_2O_4$ and Co sites of Co_3O_4. The density of states (DOS) of $NiCo_2O_4$ (c) and Co_3O_4 (d). The Gibbs free energy diagrams of the HMFCA (e) and DFF (f) paths of the HMFOR on the Ni and Co sites of $NiCo_2O_4$ and the Co sites of Co_3O_4. (g) The adsorption configurations of HMFOR intermediate HMFCA on Ni sites and Co sites of $NiCo_2O_4$ and Co sites of Co_3O_4.

$NiCo_2O_4$ adsorb from the side of HMF. The Ni sites of $NiCo_2O_4$ and the Co sites of Co_3O_4 are adsorbed from the front of HMF, and the steric hindrance is large, indicating that the Co sites of $NiCo_2O_4$ are more conducive to the formation of HMF* to accelerate the reaction, which is consistent with the previous *in situ* FTIR analysis. Compared with the HMFCA path and the DFF path, the Co site of HMF* → HMFCA* is more exothermic than the Co site of HMF* → DFF*, which is more conducive to the generation of HMFCA*, further confirming that the main path is the HMFCA path. Since FDCA* is endothermically desorbed to obtain FDCA, the Ni sites of $NiCo_2O_4$ are superior to the Co sites of $NiCo_2O_4$ and the Co sites of Co_3O_4. Combined with the adsorption configuration, it can be seen that the conversion of FDCA* to FDCA requires desorption from adjacent metal atoms, and the Ni adsorption capacity is poor, indicating that the Ni sites of $NiCo_2O_4$ are more favorable for FDCA* to form FDCA. The results show that the introduction of Ni and the synergistic effect on $NiCo_2O_4$ are beneficial to accelerate the reaction conversion rate in the RDS and HMFOR processes, thereby promoting the improvement of product selectivity and yield.

Electrocatalytic performance of the CO_2-HMF coupled system reaction

Based on $NiCo_2O_4$, a paired electrolysis system was developed with the prepared $NiCo_2O_4$ as the HMFOR anode and Au nanoparticles as the CO_2RR cathode (Fig. 5a and S34).[8,14,25] For comparison, the CO_2RR system was also compared with the traditional anode OER. The LSV curve shown in Fig. 5b shows that at the same current density, the voltage required for the CO_2-HMF coupled system is lower than that of the OER-CO_2RR system ($\Delta E = 275$ mV), indicating that the use of biomass small

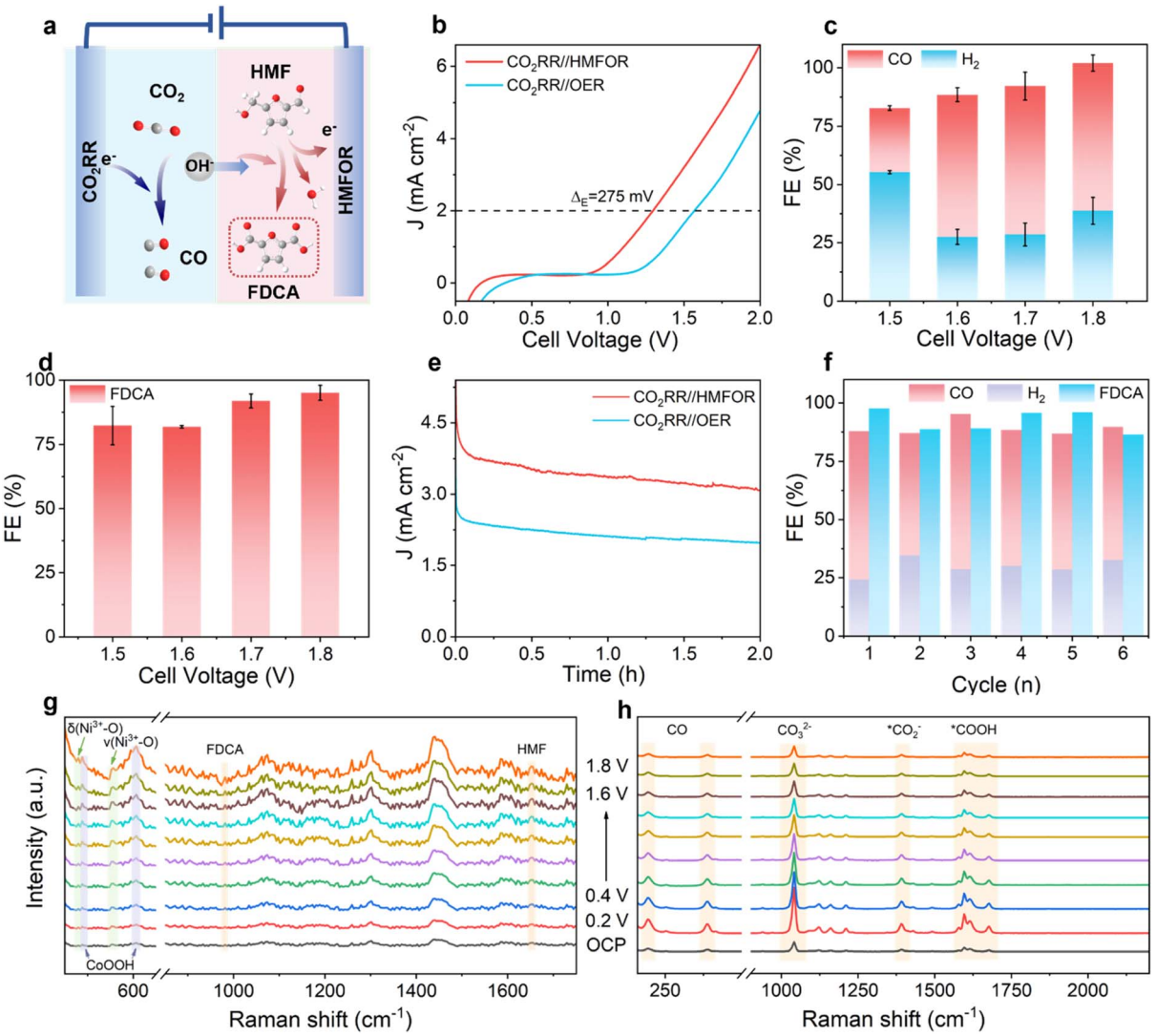

Fig. 5 (a) Integrated electrolysis cell coupling the CO_2RR-HMFOR. (b) Current density *vs.* cell voltage curves of the CO_2RR-HMFOR or OER-HMFOR. (c) CO_2RR-HMFOR cathode: FE of CO and H_2 at different cell voltages for Au. (d) CO_2RR-HMFOR anode: FE of FDCA at different cell voltages for $NiCo_2O_4$. (e) The change in current density with time during 1.7 V potentiostat electrolysis in a H-type cell. (f) Stability test of the HMFOR-CO_2RR. *In situ* Raman spectroscopy spectra of the CO_2RR-HMFOR: (g) anode reaction and (h) cathode reaction.

molecule oxidation instead of the OER can reduce the energy consumption required for the electrolysis process. The cathode and anode products of the coupled system were analyzed at 1.5–1.8 V (Fig. 5c and d). The FE_{FDCA} at the anode is higher than 86%, and the highest value reached 91.9% at 1.7 V. The selectivity of the cathode to CO also reached 69.8% at 1.7 V, the FE for CO was 66.1%, and the FE of H_2 was 28.6%. These results are among the top records for both the FE of CO_2 and HMF (Table S15). Energy efficiency (EE) is the percentage of the energy retained in the target product to the total energy input into the electrolysis system.[48] It can be used to measure the effectiveness of the reaction process that converts the input electric energy into valuable chemical products and stores it in the form of chemical energy. We calculate EE for further evaluation, and it can be seen that the total energy conversion efficiency is stable at about 43% at 1.5–1.8 V (Fig. S35). At 1.7 V, the total energy conversion efficiency is 43.3% (22.2% for FDCA, 15.9% for CO, and 5.2% for H_2), which has a good effect on achieving high energy conversion efficiency at low potential (Table S16). High EE is essential to reduce electricity costs and improve the economic benefits of the CO_2RR. In the potentiostatic electrolysis process (Fig. 5e), the change in cell current with time showed a significant difference between HMFOR-CO_2RR and OER-CO_2RR pairing systems in a H-type cell. The average current required for the CO_2-HMF coupled system is 4 mA cm^{-2}, and the average current required for the OER-CO_2RR system is 2 mA cm^{-2}. In the early stage of electrolysis of the CO_2-HMF coupled system, the current density changes rapidly. However, in the later stage, due to the consumption of HMF, the OER dominates and the current change converges with the OER. In this case, the kinetic rate of the anodic reaction becomes slow with the decrease of the reactant concentration. For the OER-

CO_2RR system, the continuous decrease in current is due to the consumption of OH^- by the OER. In addition, the system has excellent catalytic stability (Fig. 5f and S36), and the total FE exceeds 190% after 6 cycles of the stability test, and the FE_{FDCA} is stable between 86.4% and 97.6%. At the same time, the total FE of the cathode is stable at more than 86%, including CO (57.1–66.6%) and H_2 (24.2–32.6%). The stability of its structure and composition was evaluated by a series of characterization studies. In the SEM images it can be seen that the needle-like array structure of $NiCo_2O_4$ and the overall contour of Au nanoneedles are well maintained (Fig. S37). The XRD pattern shows that the anode cathode catalyst still shows the original characteristic diffraction peak, and no new peaks appear, indicating that the crystal structure of the catalyst does not change significantly after the CO_2-HMF coupled system reaction (Fig. S38).

In situ Raman spectroscopy of the coupled system

In order to detect and track the dynamic evolution of the intermediate products at both ends of the CO_2-HMF coupled system in real time, *in situ* Raman spectroscopy (SERS) can not only monitor the changes of the intermediates at both ends of the CO_2-HMF coupled system, but also analyze the changes of the surface state of the catalysts at both ends. For the HMFOR (Fig. 5g), there are two obvious peaks at 479 and 555 cm^{-1}, which are attributed to the e_g bending (δ) and A_{1g} stretching (ν) modes of Ni^{3+}–O, respectively. With the increase of applied potential, abundant NiOOH species are formed and accumulated on the electrode surface.[20,49] This phenomenon also implies that the generated Ni^{3+}–O species is an active intermediate; two obvious peaks at 487 and 606 cm^{-1} are attributed to CoOOH, which accumulates with the increase of applied potential as NiOOH species, while the signal peak of CoO_2 is almost undetectable, indicating that Co^{3+} is the active site of the HMFOR.[31] At the same time, with the increase of the potential, the HMF (1653 cm^{-1}) peak gradually increases, indicating that the adsorption of HMF is continuously enhanced, which is consistent with the previous characterization results. The peak of FDCA (982 cm^{-1}) also gradually increases, and the generation of FDCA is positively correlated with the applied potential, which is consistent with Fig. 5d.[50,51] This shows that the two-site synergy of $NiCo_2O_4$ is applied to high-efficiency HMFOR, which further confirms the reliability of the theoretical calculation results. For the CO_2RR (Fig. 5h), the peaks at 195 and 388 cm^{-1} correspond to the restricted rotation and Au–CO stretching of adsorbed CO, respectively.[52] As the potential increases, the CO coverage decreases and Au accelerates CO desorption. No *CO peak at 2100 cm^{-1} verifies this conjecture. At the same time, $*CO_2^-$ (1394 cm^{-1}) and *COOH (1563–1686 cm^{-1}) are necessary intermediates for the formation of *CO.[53,54] As the potential increases, the peak intensity decreases, which is related to the decrease of CO selectivity, which is consistent with the Fig. 5c results. Overall, in the CO_2RR-HMFOR coupled system, the $NiCo_2O_4$ anode promotes HMF-to-FDCA conversion *via* potential-dependent formation of Ni^{3+} and Co^{3+} intermediates for OH^- capture. Meanwhile, the key intermediates of the CO_2-to-CO conversion are observed at the cathode. The simultaneous progress of these anodic and cathodic reactions significantly reduces the overall energy consumption of the process.

Conclusions

In summary, we present a cobalt-based spinel anode catalyst with a Ni–Co dual-site synergistic effect, which achieves efficient and stable electrochemical HMFOR under alkaline conditions, delivering a high FE_{FDCA} of 99.1% at 1.5 V *vs.* RHE. Comprehensive characterization confirms that the introduction of Ni significantly enhances the adsorption and conversion capability of the catalyst towards HMF and OH^- species. This enhancement is particularly crucial in the key FFCA → FDCA conversion step, effectively facilitating dehydrogenation and electron transfer processes. In the coupled system, at a cell voltage of 1.7 V, the anode maintains a high FE_{FDCA} of 91.9%, while the cathode FE is 94.7% (CO is 66.1% and H_2 is 28.6%), and the total energy conversion efficiency is 43.3%. SERS and DFT are used to reveal the dynamic catalytic mechanisms in the CO_2-HMF coupled system. The $NiCo_2O_4$ anode promotes HMF-to-FDCA conversion *via* potential-dependent formation of Ni^{3+} and Co^{3+} intermediates for OH^- capture. Meanwhile, the key intermediates of the CO_2-to-CO conversion are observed at the cathode, offering a real-time experimental basis for optimizing such integrated electrocatalytic systems for concurrent CO_2 and biomass conversion. This work provides compelling experimental evidence for the co-production of high-value chemicals *via* the upgrading of biomass-derived platform molecule HMF and CO_2 conversion. More importantly, the adopted electronic structure regulation strategy and the established *in situ* dynamic monitoring method provide a universal research paradigm and technical path for the design and optimization of other coupled electrosynthesis systems (such as glycerol, ethanol, benzyl alcohol, *etc.*) involving organic molecule oxidation and CO_2 reduction.

Author contributions

Z. L. and T. O. conceived and supervised the research and performed funding acquisition and writing – review & editing. Q. Y. conducted the experiments, analyzed the data, and wrote the manuscript. X. L. assisted with the material synthesis and characterization. J. L. supported supervising and reviewing the manuscript. All authors contributed to the interpretation of the results.

Conflicts of interest

There are no conflicts to declare.

Data availability

All the data supporting this article have been included in the main text and the supplementary information (SI). Supplementary information: detailed experimental methods (catalyst synthesis, characterization techniques, electrochemical testing,

and product analysis), supplementary figures (materials characterization, electrochemical performance data, *in situ* spectroscopy results, and computation l models), and supplementary tables (EIS fitting parameternsive DFT calculation data) that support the findings discussed in the main text. Supplementary information is available. See DOI: https://doi.org/10.1039/d5sc10014.

Acknowledgements

This work was financially supported by the National Natural Science Foundation of China (No. 22379033, U24A20541 and 22278094), National Key Research and Development Program Project (No. 2025YFF0516504), Guangdong Basic and Applied Basic Research Foundation (No. 2025B1515020046), Guangzhou Science and Technology Program (No. 2025A03J0011), Basic and Applied Basic Research Program of Guangzhou (No. 2024A03J0236), and Open Project of State Key Laboratory of Inorganic Synthesis and Preparative Chemistry (2026-09). We would like to thank the Analysis and Test Center of Guangzhou University for their technical support.

Notes and references

1 S. W. Boettcher, *Chem. Rev.*, 2024, **124**, 13095–13098.
2 L. Lin, P. Su, Y. Han, Y. Xu, Q. Ni, X. Zhang, P. Xiong, Z. Sun, G. Sun and X. Chen, *eScience*, 2025, **5**, 100264.
3 Z. Deng, B. Zhu, S. J. Davis, P. Ciais, D. Guan, P. Gong and Z. Liu, *Nat. Rev. Earth Environ.*, 2025, **6**, 231–233.
4 T. Liu, H. Luo, T. Ouyang and Z. Liu, *Adv. Funct. Mater.*, 2025, **35**, 2415367.
5 R. Zhao, Z. Zhu, T. Ouyang and Z. Liu, *Angew. Chem., Int. Ed.*, 2024, **63**, e202313597.
6 T. Xiang, T. Liu, T. Ouyang, S. Zhao and Z. Liu, *Interdiscip. Mater.*, 2024, **3**, 380–388.
7 R. Zhao, H. Luo, T. Ouyang and Z.-Q. Liu, *ACS Nano*, 2024, **18**, 35749–35757.
8 F. Ye, S. Zhang, Q. Cheng, Y. Long, D. Liu, R. Paul, Y. Fang, Y. Su, L. Qu, L. Dai and C. Hu, *Nat. Commun.*, 2023, **14**, 2040.
9 H. Wu, L. Huang, J. Timoshenko, K. Qi, W. Wang, J. Liu, Y. Zhang, S. Yang, E. Petit, V. Flaud, J. Li, C. Salameh, P. Miele, L. Lajaunie, B. Roldán Cuenya, D. Rao and D. Voiry, *Nat. Energy*, 2024, **9**, 422–433.
10 X. Li, Q. Chen, W. Sun, C. He and Z. Wen, *Angew. Chem., Int. Ed.*, 2024, **63**, e202412410.
11 S.-Q. Liu, M.-R. Gao, S. Wu, R. Feng, Y. Wang, L. Cui, Y. Guo, X.-Z. Fu and J.-L. Luo, *Energy Environ. Sci.*, 2023, **16**, 5305–5314.
12 S. Liu, B. Tian, X. Xu, X. Wang, P. Ran, Y. Sun, J. Wu, A. Qiu, F. Wang, L. Tang, J. Ma and M. Ding, *ACS Catal.*, 2024, **14**, 9476–9486.
13 X. Jiang, K. Zhao, H. Feng, L. Ke, X. Wang, Y. Liu, L. Li, P. Sun, Z. Chen, Y. Sun, Z. Wang, L. Yu and N. Yan, *J. Am. Chem. Soc.*, 2025, **147**, 13471–13482.
14 W. Guo, X. Cao, D. Tan, B. Wulan, J. Ma and J. Zhang, *Angew. Chem., Int. Ed.*, 2024, **63**, e202401333.
15 C. Lu, P. Shi, S. Huang, C. Yang, J. Zhu, J. Zhang, C. Ke, Y. Su, X. Zhuang and T. Wang, *Angew. Chem., Int. Ed.*, 2025, **64**, e202423263.
16 C. Lu, S. Yang, P. Shi, S. Huang, C. Cai, J. Zhu, X. Zhuang and T. Wang, *Angew. Chem., Int. Ed.*, 2025, **64**, e202502846.
17 L. Chen, C. Yu, X. Song, J. Dong, J. Mu and J. Qiu, *Nat. Commun.*, 2024, **15**, 8072.
18 D. Chen, W. Li, J. Liu and L. Sun, *Energy Environ. Sci.*, 2025, **18**, 3120–3128.
19 L. Zeng, Y. Chen, M. Sun, Q. Huang, K. Sun, J. Ma, J. Li, H. Tan, M. Li, Y. Pan, Y. Liu, M. Luo, B. Huang and S. Guo, *J. Am. Chem. Soc.*, 2023, **145**, 17577–17587.
20 J. Woo, J. Choi, J. Choi, M. Lee, E. Kim, S. Yun, S. Yoo, E. Lee, U. Lee, D. H. Won, J. H. Park, Y. J. Hwang, J. S. Yoo and D. K. Lee, *Adv. Funct. Mater.*, 2025, **35**, 2413951.
21 Y. Lu, T. Liu, C. Dong, C. Yang, L. Zhou, Y. Huang, Y. Li, B. Zhou, Y. Zou and S. Wang, *Adv. Mater.*, 2022, **34**, 2107185.
22 M. Zubair, P. M. Usov, H. Ohtsu, J. A. Yuwono, C. S. Gerke, G. D. Y. Foley, H. Hackbarth, R. F. Webster, Y. Yang, W. H. Lie, Z. Ma, L. Thomsen, M. Kawano and N. M. Bedford, *Adv. Energy Mater.*, 2024, **14**, 2400676.
23 L. Zhang, P. Jin, Z. Wu, B. Zhou, J. Jiang, A. Deng, Q. Li, T. Hussain, Y. Zhang, H. Liu and S. Wang, *Energy Environ. Mater.*, 2024, **7**, e12725.
24 X. Jiang, X. Ma, Y. Liu, L. Zhao, Y. Zhang, B.-Q. Li and Q. Zhang, *Appl. Catal., B*, 2024, **347**, 123785.
25 X. Liu, Y. Zhang, Y. Li, B. Yan and X. Zhao, *Appl. Catal., B*, 2025, **368**, 125146.
26 J. Bi, Q. Zhu, W. Guo, P. Li, S. Jia, J. Liu, J. Ma, J. Zhang, Z. Liu and B. Han, *ACS Sustain. Chem. Eng.*, 2022, **10**, 8043–8050.
27 X. Cao, B. Wulan, Y. Wang, J. Ma, S. Hou and J. Zhang, *Sci. Bull.*, 2023, **68**, 1008–1016.
28 S. Liu, B. Zhang, Y. Cao, H. Wang, Y. Zhang, S. Zhang, Y. Li, H. Gong, S. Liu, Z. Yang and J. Sun, *ACS Energy Lett.*, 2023, **8**, 159–168.
29 J. Ma, X. Wang, J. Song, Y. Tang, T. Sun, L. Liu, J. Wang, J. Wang and M. Yang, *Angew. Chem., Int. Ed.*, 2024, **63**, e202319153.
30 G. Zhao, G. Hai, P. Zhou, Z. Liu, Y. Zhang, B. Peng, W. Xia, X. Huang and G. Wang, *Adv. Funct. Mater.*, 2023, **33**, 2213170.
31 X. Deng, G. Xu, Y. Zhang, L. Wang, J. Zhang, J. Li, X. Fu and J. Luo, *Angew. Chem., Int. Ed.*, 2021, **60**, 20535–20542.
32 H. G. Xu, X. R. Ning, J. Y. Zhao, H. Y. Lin, H. Q. Fu, S. Wang, Y. Guo, H. Wu, M. Zhu, H. Y. Yuan, P. F. Liu and H. G. Yang, *Chem*, 2024, **10**, 2147–2169.
33 Y. Lu, C. Dong, Y. Huang, Y. Zou, Z. Liu, Y. Liu, Y. Li, N. He, J. Shi and S. Wang, *Angew. Chem., Int. Ed.*, 2020, **59**, 19215–19221.
34 Q. Hu, S. Qi, Q. Huo, Y. Zhao, J. Sun, X. Chen, M. Lv, W. Zhou, C. Feng, X. Chai, H. Yang and C. He, *J. Am. Chem. Soc.*, 2024, **146**, 2967–2976.
35 X. Wang, T. Ouyang, L. Wang, J. Zhong, T. Ma and Z. Liu, *Angew. Chem., Int. Ed.*, 2019, **58**, 13291–13296.
36 Y. Liu, X. Ren, J. Wang, H. Wang, Z. Yin, Y. Wang, W. Huang, X. Hu, Z. J. Xu and Y. Deng, *J. Am. Chem. Soc.*, 2025, **147**, 20318–20328.

37 Y. Zhang, Q. Wu, J. Z. Y. Seow, Y. Jia, X. Ren and Z. J. Xu, *Chem. Soc. Rev.*, 2024, **53**, 8123–8136.
38 P. Xu, Z. Bao, Y. Zhao, L. Zheng, Z. Lv, X. Shi, H. Wang, X. Fang and H. Zheng, *Adv. Energy Mater.*, 2024, **14**, 2303557.
39 C. Xu, E. Paone, D. Rodríguez-Padrón, R. Luque and F. Mauriello, *Chem. Soc. Rev.*, 2020, **49**, 4273–4306.
40 M. Qin, J. Chen, M. Qi, H. Wang, S. Mao, L. Xi and Y. Wang, *ACS Catal.*, 2024, **14**, 8414–8426.
41 J. Zhang, Y. Shen, Z. Wu, X. Zhang, J. Kang, Y. Wu, S. Zhang, S. Chen, G. Wang, H. Zhang, H. Yin and H. Zhao, *Angew. Chem., Int. Ed.*, 2025, **64**, e202423109.
42 C. Wang, Z. Zhao, W. Cao, Y. Peng, M. Song and Y. Wu, *Adv. Funct. Mater.*, 2025, 2502618.
43 P. Zhou, X. Liu, Z. Chen, C. Tang, X. Zhao, J. Zheng, R. Ge and H. Duan, *Adv. Funct. Mater.*, 2025, 2502081.
44 A. Prajapati, N. Govindarajan, W. Sun, J. Huang, H. Bemana, J. T. Feaster, S. A. Akhade, N. Kornienko and C. Hahn, *ACS Catal.*, 2024, **14**, 10122–10131.
45 P. Zhou, X. Lv, S. Tao, J. Wu, H. Wang, X. Wei, T. Wang, B. Zhou, Y. Lu, T. Frauenheim, X. Fu, S. Wang and Y. Zou, *Adv. Mater.*, 2022, **34**, 2204089.
46 K. Wang, M. Wu, Y. Zhang, B. Jiang, Y. Su, S. Yang, X. Lu and H. Li, *Adv. Funct. Mater.*, 2025, **35**, 2424435.
47 Y. Ma, Y. Xiao, C. Lei, X. Zhang, W. Sheng, S. Liu, P. Chen, P. Zhou, H. Duan, P. Li and M. Gong, *Adv. Funct. Mater.*, 2025, e12292.
48 W. Lai, Y. Qiao, J. Zhang, Z. Lin and H. Huang, *Energy Environ. Sci.*, 2022, **15**, 3603–3629.
49 H. Zhang, Q. Yang, S. Luo, Z. Liu, J. Huang, Y. Zheng, C. Hu, J. Zhang, X. Bao, P. Yuan and X. Yao, *ACS Catal.*, 2024, **14**, 9565–9574.
50 G. Fu, X. Kang, Y. Zhang, Y. Guo, Z. Li, J. Liu, L. Wang, J. Zhang, X.-Z. Fu and J.-L. Luo, *Nat. Commun.*, 2023, **14**, 8395.
51 T. Huang, J. Han, Z. Li, Y. Hong, X. Gu, Y. Wu, Y. Zhang and S. Liu, *Angew. Chem., Int. Ed.*, 2025, **64**, e202500269.
52 D. Zhang, X. Liu, Y. Zhao, H. Zhang, A. V. Rudnev and J.-F. Li, *Chem. Sci.*, 2025, **16**, 4916–4936.
53 M. Zheng, P. Wang, X. Zhi, K. Yang, Y. Jiao, J. Duan, Y. Zheng and S.-Z. Qiao, *J. Am. Chem. Soc.*, 2022, **144**, 14936–14944.
54 M. Wang, M. Fang, Y. Liu, C. Chen, Y. Zhang, S. Jia, H. Wu, M. He and B. Han, *J. Am. Chem. Soc.*, 2025, **147**, 16450–16458.